



Universidad Autónoma
de Madrid

Biblos-e Archivo
Repositorio Institucional UAM

Repositorio Institucional de la Universidad Autónoma de Madrid

<https://repositorio.uam.es>

Esta es la **versión de autor** del artículo publicado en:
This is an **author produced version** of a paper published in:

Spectrochimica Acta Part A: Molecular and Biomolecular Spectroscopy 205 (2018):
489-496

DOI: <https://doi.org/10.1016/j.saa.2018.07.072>

Copyright: © 2018 Elsevier B.V. All rights reserved

This manuscript version is made available under the CC-BY-NC-ND 4.0 licence
<http://creativecommons.org/licenses/by-nc-nd/4.0/>

El acceso a la versión del editor puede requerir la suscripción del recurso
Access to the published version may require subscription

Spectroscopic analysis of corrosion products in a bronze cauldron from the Late Iberian Iron Age

Daniel Cosano,^a Dolores Esquivel,^a Laura D. Mateos,^a Fernando Quesada,^b César Jiménez-Sanchidrián,^a José Rafael Ruiz^{a,*}

^aDepartamento de Química Orgánica, Universidad de Córdoba, Campus de Rabanales, Edificio Marie Curie. Carretera Nal. IV-A km. 396, 14071 Córdoba (Spain)

^bDepartamento de Prehistoria y Arqueología, Facultad de Filosofía y Letras, Universidad Autónoma de Madrid, Campus de Cantoblanco, 28049 Madrid (Spain)

* Corresponding author. E-mail address: go1ruarj@uco.es. Phone no.: 34 957 218638. Fax no.: 34 957212066

Selected bronze fragments unearthed at Cerro de la Cruz (Almedinilla, southern Spain) were analysed to determine the chemical composition of the corrosion products formed on their surface. The fragments came from a large bronze cauldron used in an Iberian village that was devastated in the mid II century b.C. —possibly around 141 b.C. The fragments were analysed by using various instrumental techniques including electron scanning microscopy coupled to energy dispersive X-ray spectroscopy (SEM–EDS), X-ray fluorescence (XRF) spectroscopy, and also by X-ray diffraction (XRD) and micro-Raman spectroscopy. Based on the results, being buried for a long time caused the main elements in the alloy to mineralize and form stratified layers consisting of various mineral phases including cuprite (Cu_2O), malachite [$\text{Cu}_2\text{CO}_3(\text{OH})_2$] and cassiterite (Sn_2O). The fragments also contained chloride and trihydroxychloride compounds such as nantokite (CuCl) and atacamite [$\text{Cu}_2\text{Cl}(\text{OH})_3$], respectively, which make conservation of archaeological objects troublesome. These results testify to a strong interaction of the alloy elements with soil components. Also, the results obtained suggest a Type I of corrosion structure. Using the SEM–EDS, XRD and XRF and micro-Raman spectroscopies allowed corrosion products in the fragments to be successfully characterized in microchemical and structural.

Keywords: Bronze, corrosion, micro-Raman spectroscopy, XRF, atacamite, malaquite, cuprite.

1. Introduction

Bronze is a copper-tin alloy that has been one of the most widely used materials for making a variety of household utensils since ancient times [1]. Sometimes, bronze contains other elements such as lead at variable concentrations [2]. Tin is typically used for greater hardness and lead to increase porosity. In an aggressive environment (e.g., burial environment of soil environment), bronze undergoes gradual corrosion and forms a usually brownish green or greenish blue coating called a “patina”. The coating can contain various copper salts depending on where the alloy has been. For example, prolonged burial in soil causes morphologically different corrosion, from a thin corrosion layer to a completely corroded and mineralized artefact [3]. Thus, earth-buried bronze typically forms carbonates such as malachite $\text{Cu}_2\text{CO}_3(\text{OH})_2$. The presence of chloride ions in soil may lead to formation of nantokite (CuCl). This compound, during burial or after excavation, can form copper trihydroxichlorides (atacamite or paratacamite) in the presence of oxidants conditions and moisture [4]. in the air, however, bronze forms sulphates such as brochantite $[\text{CuSO}_4 \cdot 3\text{Cu}(\text{OH})_2]$, and in sea water or chloride-rich environments it forms chlorides such as atacamite $[\text{Cu}_2\text{Cl}(\text{OH})_3]$. The patina usually coats a red layer of cuprous oxide in contact with the alloy metal core [5-7]. The presence of sulphide ions in the medium causes the formation of copper or lead sulphides [8].

The corrosion compounds formed in bronze objects can be studied by using various instrumental techniques. In recent times, vibrational (Raman and IR) spectroscopies and microspectroscopies have proved highly effective for archaeological characterization purposes [9-17]. For example, our group has successfully used Raman spectroscopy to characterize the pigments in Roman wall paintings [18] and to identify those used in statues from also Roman times [19].

Raman spectroscopy and other instrumental techniques have greatly facilitated the duty of museum restorers and curators in preventing degradation of archaeological heritage, whether exhibited or otherwise. Metal objects require special care as they can easily corroded and bronze objects abound in museum collections throughout the world as a result of the alloy

being used since the dawn of mankind to make not only everyday objects but also statues, architectural elements and monuments.

In this work, the objective was study the patina on an Iberian cauldron found at Cerro de la Cruz, archaeological site in Almedinilla (southern Spain) in order to identify the corrosion products formed, so that later restoration professionals can choose the most appropriate procedure for its conservation. For this purpose, fragments of the cauldron were characterized by scanning electron microscopy–energy dispersive X-ray spectroscopy (SEM–EDS), X-ray diffraction (XRD) and Raman microspectroscopy.

Archaeological context of the cauldron

Cerro de la Cruz, located in Almedinilla (a population in the province of Cordoba, southern Spain) is an *oppidum* (i.e., a fortified town from Iberian culture, which spanned the centuries V to I b.C.). The site has been known since the XIX century but was not thoroughly and scientifically excavated until fairly recently (specifically, over the periods 1985–90 [20] and 2006–2010 [21]). It spans an area of ca. 3.5 ha and is thus mid-sized among Iberian archaeological sites. The studied stage was that of the eventual destruction of the original village, which probably occurred during the campaigns of the Roman consul Servilianus in 141 b.C. as told by the Greek author Appian [22]. The initially estimated date, based on local and foreign ceramics and coins, was confirmed by carbon-14 analysis.

The village houses, made of stone and mudbrick, comprised two floors plus a terrace and collapsed under fire. The skeletons of two mutilated corpses were found on the streets and various other human remains encountered among the rubble [21]. Some grain mills were working at the time the village was destroyed [23]. Fire lasted a long time and the resulting rubble was not subsequently removed; as a result, all remains (ceramics, food, tools) were sealed under mudbrick rubble.

The bronze cauldron studied was found in room III, a quadrangular space directly accessed from main street XXV. It was scrambled with many other objects including a lead cup which had melted under the heat, and many amphorae and other ceramic vessels, in the building's collapse rubble. The building's ground floor was used to store grain (particularly barley) in

amphorae. As can be seen in Fig. 1, the cauldron, made of copper alloy, was severely smashed and distorted by the collapsing building (Fig. 2). It was probably hemispherical in shape and about 38.2 cm in rim diameter. The cauldron showed signs of repair with rivets (Fig. 2c); also, it contained imprinted organic material (Fig. 2b) —possibly esparto or some rough fabric [21]. It was used mainly to cook meat [22] but may also have been employed for other purposes.

2. Materials and methods

One side of the fragments examined in this work had abundant adhered material whereas the other was virtually clean. The cauldron surface was greenish on both sides but lighter on the clean side. Under a light microscope, the cross-section of each fragment was found to contain a red-coloured central layer accompanied by another consisting of a mixture of greyish, greenish and reddish hues (Fig. 3). In all cases, different fragments were analyzed, corresponding to significant parts of the cauldron.

The chemical composition and nature of the corrosion products in the fragments was determined by scanning electron microscopy–energy dispersive X-ray spectroscopy (SEM–EDS), X-ray diffraction and Raman microspectroscopy.

Scanning electron micrographs and energy-dispersive spectra were obtained with a JEOL JSM 6300 microscope interfaced to an X-act 80 semi-quantitative elemental microanalyser.

To check the chemical composition of the cauldron, X-ray fluorescence (XRF) spectroscopy was used. Spectra were acquired with a Rigaku ZSK PrimusIV wavelength X-ray spectrometer. The system is equipped with a 3 kW Rh-target X-ray tube, ten analyzer crystal, a sealed proportional counter for light elements detection and a scintillation counter for heavy elements. For analysis of elemental distributions along a line (i.e. line scan) of the cauldron, a MAXXI 6 Coating Thickness Analyser from Hitachi High-Tech Analytical Science was used. The angle of incidence of the SR beam was 45° and the energy dispersive (Röntec) fluorescence detector was positioned normal to the beam in the horizontal plane.

X-ray diffraction patterns were obtained with a Bruker D8 Advance diffraction spectrometer equipped with a goniometer and a DACO-MP automated data acquisition system. Samples were irradiated with light from the K α line of copper ($\lambda = 1.54 \text{ \AA}$). The spectrometer

was furnished with a nickel filter and a graphite monochromator. The goniometer speed was 2 °/min. Some samples were ground to a small enough grain size in an agate mortar prior to analysis. Then, an appropriate amount of powder was placed on a plastic slide and compressed to ensure that the light-exposed surface would be as flat and uniform as possible.

Raman spectra were recorded on a Renishaw spectrometer (InVia Raman Microscope) equipped with a Leica microscope with various lenses, monochromators, filters and a CCD detector. Spectra were recorded over the wavenumber range 150–1700 or 150–4000 cm^{-1} upon excitation with green laser light. The number of spectra recorded in each run differed with the experimental conditions. In any case, the primary aim was to maximize the signal-to-noise ratio. As for the XRD patterns, some samples were ground in an agate mortar prior to recording of their spectra.

3. Results and discussion

3.1. SEM-EDS.

The surface of the cauldron fragments consisted of corrosion layers and adhered debris from the material under which they were buried. The debris was largely on one side and covered virtually the whole fragment surface. Observation under a light microscope of the fragment cross-sections revealed the presence of a greenish–reddish–greyish layer and a reddish layer, and provided an indication of their thickness. As can be seen from the micrograph of Fig. 3, the whole object was corroded; also, it exhibited no trace of the original metal structure. The corrosion layers and their sequence were similar in all fragments.

Each of the four layers was subjected to semi-quantitative analysis by EDS to determine their elemental composition. Figure 4 shows the four zones in the scanning electron micrograph obtained, namely: (A) a green outer layer containing abundant adhered debris, (B) a greenish–reddish–greyish inner layer, (C) a reddish inner layer and (D) a green outer layer containing less adhered debris. Table 1 summarizes the results of the analysis. Because the results for each layer were similar among fragments, the table shows the average value for each quantity. Interestingly, all layers contained silicon, most probably from adhered debris; however, the amount of silicon present was much smaller in layers A and D than it was in B and C. Also, the

two outer layers differed markedly in chemical composition. Thus, tin and chlorine were only detected in C and D; also, chloride was present in much greater amounts in D than in C.

These results suggest that corrosion developed differently on the outer and inner side of the cauldron. One should bear in mind that the corrosion morphology of buried bronze objects depends to a great extent on the particular physico-chemical conditions of the environment (especially on pH, chemical composition, moisture content and degree of aeration) [23]. Thus, copper oxidation in alkaline earth causes the formation of cuprite (Cu_2O), which can be further transformed into malachite [$\text{Cu}_2\text{CO}_3(\text{OH})_2$] at the surface. Malachite is the end-product of the reaction of cuprite with carbonate and/or bicarbonate ions dissolved in ground water [24]. Malachite thus formed eventually coats the object with a green patina. In the presence of chloride ions, however, copper is oxidized to nantokite (CuCl), according to the process:



Air and moisture make this compound highly unstable and cause its transformation into atacamite [$\text{Cu}_2(\text{OH})_3\text{Cl}$], whether in the ground or after unearthing:



The latter process is known as “bronze disease” and develops until all metal has been corroded [2]. It is therefore crucial to avoid bronze disease in order to effectively restore and conserve corroded bronze archaeological objects, which this requires a sound knowledge of the chemical composition of each coating.

3.2. *XRF spectroscopy*

To confirm the data obtained by SEM-EDX, we have conducted a study by X-ray fluorescence (XRF) spectroscopy. This study has been done in two ways. In the first place, different representative samples of the cauldron have been taken and its chemical composition analyzed. The results obtained are shown in table 2. These values are quantitative and, unlike those obtained by SEM-EDX, they provide the total composition of the different elements without determining the layer in which they are found. The main element is copper. Important amounts of silicon, calcium and tin are also determined. Smaller, but also significant amounts of chlorine and antimony, and aluminum and magnesium oxides, have been determined. These

data are in agreement with those obtained by SEM-EDX. Also, to confirm the presence of these elements in the different layers of the cauldron, an analysis of elemental distribution along a line of the cross-sections of the cauldron was also carried out using this XRF technique. Figure 5 shows the results obtained for tin. The analysis indicates that the external face without adhered debris has less than 1% tin. The face with adhered debris presents around 20% of the total tin, while in the inner layer most of this element is found (approximately 80%). Therefore, these results confirm those obtained by SEM-EDS. It has also been found (results not shown) that chlorine is only detected in the same layers as tin. Calcium is found mostly in the face with abundant adhered debris, while copper is uniformly distributed.

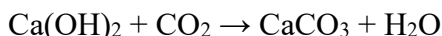
3.3. *XRD Analysis of corrosion products*

Identifying the compounds in corrosion coatings by XRD spectroscopy is often a complex, labour-intensive task owing to their typically low crystallinity [26].

The XRD study was performed on powdered samples from several fragments in order to identify as many compounds as possible. Figure 6 shows the XRD pattern for one of the samples, which was similar to those for all others. Some of the strongest lines allowed three corrosion products to be identified, namely: cuprite (Cu_2O), atacamite [$\text{Cu}_2\text{Cl}(\text{OH})_3$] and nantokite (CuCl). Other, weaker lines, were assigned to malachite [$\text{Cu}_2\text{CO}_3(\text{OH})_2$]. There were additional strong lines due to calcite and several weaker lines that could not be unequivocally assigned but might be due to contaminants in adhered debris.

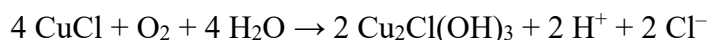
As shown by the SEM-EDS analysis, the composition of the corrosion layers differed between the two sides of the cauldron. This led us to examine both sides by XRD spectroscopy. As can be seen, the XRD patterns confirmed the previous results and were completely different for the two sides —only the region from 10 to 50° is shown in the figure, however. The “cleaner” side (viz., that containing no adhered debris) exhibited a rather complex XRD pattern which, however, allowed atacamite, cuprite, nantokite and brochantite to be identified. The patterns contained additional, weaker lines for calcite and malachite. On the other hand, the strongest lines in the XRD pattern for the debris-coated side of the cauldron were those for calcite (CaCO_3) —from adhered debris— and malachite. These results suggest that the

cauldron was probably standing on the ground when the room collapsed, and also that one side was exposed to corrosive agents in the earth whereas the other was buried by rubble. The fact that the debris was rich in calcium carbonate is unsurprising because Iberian mortars consisted mostly of lime, sand and water. Carbonate formed from lime $[\text{Ca}(\text{OH})_2]$ was used as a binder in the mortars. Thus, as calcium hydroxide dries, it hardens and is carbonated by atmospheric carbon dioxide as follows:



Another possible origin of this calcium carbonate could be the use of the cauldron as a vessel for some works in relation with calcite or carbonate compounds, for example to prepare pigments or plaster.

The carbonate also resulted in the formation of different corrosion products on each side of the cauldron. Thus, the major corrosion product on the side in contact with the rubble, which was rich in calcium carbonate, was malachite. On the other hand, the major corrosion product on the side in contact with the ground was atacamite—which suggests the presence of chloride ions. However, neither malachite nor atacamite are primary corrosion products. Thus, as stated in the Introduction, malachite forms from cuprite in the presence of carbonate ions, whereas atacamite results from nantokite, a cuprous chloride formed in the presence of chloride ions. Over time (while the cauldron was buried or even after surfacing), nantokite was possibly transformed into atacamite in a process known as “bronze disease” that requires the presence of oxygen and water [29]:



3.4. *Raman analysis of corrosion products*

To corroborate the results obtained after the analysis by XRD, we have used a supplementary molecular characterization technique such as Raman spectroscopy [28-31], which is especially by virtue of its non-destructive nature, high spatial resolution and ability to detect amorphous or poorly crystalline phases. Unlike XRD, this technique allowed different spots in each fragment to be examined on an individual basis. The micrograph of Fig. 3 is a cross-sectional view of one fragment. The spectra for the inner reddish layer in all fragments,

Fig. 8, were consistent with the presence of cuprite (the inset shows the point where the spectrum was recorded). The strong band at 217 cm^{-1} , and the weaker ones at 202 (a shoulder), 621, 285, 408 and 331 cm^{-1} , clearly indicate the presence of cuprite. Cassiterite exhibits a typical Raman band at 634 cm^{-1} ; however, identifying tin with this technique is difficult because tin oxide formed by oxidation of copper-alloyed tin has a different Raman spectrum. Thus, the band corresponding to the A_{1g} vibration mode in SnO_2 , which appears at 634 cm^{-1} , shifts to smaller wavenumbers with increasing amount of copper present in the alloy (down to 634 cm^{-1} with 10% copper). According to Pagnier et al. [32], the shift is a result of the band for CuO overlapping with that for SnO_2 . Based on these results, and on those previously obtained by SEM-EDS and XRD spectroscopy, the red coating consisted of cuprite and cassiterite. The EDS results additionally suggest the presence of chlorine and sulphur in this layer. However, the XRD patterns suggested the presence of nantokite, which was not confirmed by the Raman spectra. Thus, the Raman spectrum for nantokite exhibited a strong band at 463 cm^{-1} due to symmetric stretching in Cu-Cl bonds in addition to another one at 206 cm^{-1} assigned to Cl-Cu-Cl deformation [6]. The presence of sulphur might be due to that of brochantite, which was identified in the XRD patterns but, again, not confirmed by the Raman spectra.

The Raman spectra for the two green coatings differed. Based on them, the coating with less debris was carbon-free but contained 8% chlorine and 16% oxygen, which suggests the presence of oxychlorinated species. The Raman spectra obtained at different points in the fragment were similar to that of Fig. 9a and consistent with the presence of atacamite $[\text{Cu}_2\text{Cl}(\text{OH})_3]$. In fact, the four strong bands at 972, 909, 818 and 513 cm^{-1} , and the shoulder at 831 cm^{-1} , can be assigned to this compound —and so can other, weaker bands at 453, 421, 360 and 270 cm^{-1} [33]. The spectral region from 3300 to 3550 cm^{-1} contained another three typical bands for atacamite [33]. The EDS analysis of the layer (Table 1) revealed the presence of 6% tin. In fact, the spectral band at 630 cm^{-1} was consistent with the presence of cassiterite (Sn_2O) [34]. Finally, the band ca. 460 cm^{-1} was assigned to nantokite (CuCl). The micrograph for the sample exhibited bright spots whose Raman spectra contained a strong band at 292 cm^{-1} and two weaker ones at 332 and 619 cm^{-1} (fig. 9b) Copper (II) oxide has three Raman-active vibration modes that coincide with those identified in our spectra and can thus be assigned to

tenorite (CuO) even though the XRD pattern showed none of the reflection lines for this compound. In any case, tenorite was present in small amounts since the bright spots containing it only became apparent after careful observation of the fragment under the microscope.

The other green coating, which was that containing the greatest amount of debris, was examined by Raman microspectroscopy. The results departed markedly from the previous ones. Thus, the spectra for different green-coloured spots were similar to that of Figure 10, whose bands are fully consistent with those for malachite $[\text{Cu}_2\text{CO}_3(\text{OH})_2]$ [35]. In fact, malachite exhibits strong Raman bands at 3380, 3322, 1493, 431 and 179 cm^{-1} in addition to several weaker ones at 1367, 1092, 1062, 753, 718, 535, 353, 269 and 218 cm^{-1} . The insets in the figure show the bands for the spectral region $3200\text{--}3500\text{ cm}^{-1}$ and the point where the spectrum was obtained. As previously revealed by the EDS analysis, this green coating contained large amounts of carbon and calcium. The analyses performed at different points were consistent with the presence of both carbon (black spots) and calcium carbonate (clearly visible white zones) [36,37]. Figure 11 shows the spectra for both compounds in the above-mentioned region. The presence of calcium carbonate is unsurprising because the cauldron was found under collapse rubble from an Iberian house and Iberian buildings were typically made with lime-based mudbricks.

According to Robbiola et al. [38], two types of morphology and mechanisms of formation of natural patinas on copper-tin alloys are possible. Type I structure (even surfaces or passive layers) supposes an internal tin oxidation and a selective copper dissolution. For Type II structure the corrosion process is controlled by mass transportation of negative species from the soil. The results obtained in this work suggests a Type I structure.

4. Conclusions

The experimental results obtained by using various techniques in this work reveal that the studied cauldron fragments were completely corroded and contained no traces of the original alloy. The fragments essentially contained four different layers, namely:

- Two inner layers, one of reddish hue formed by cuprite, and another one of greenish-reddish-greyish hue, rich in cuprite but also containing some cassiterite and brochantite.
- Two green outer layers differing markedly in composition (one consisted largely of atacamite in addition to smaller amounts of nantokite and tenorite, whereas the other consisted of malachite).

These results suggest that corrosion developed differently on each side of the cauldron. One plausible explanation is provided by available archaeological information for the site. Thus, there is solid evidence that the Iberian village where the cauldron was found was devastated; as a result, the cauldron was buried under collapse rubble from a hut. At the time, buildings were made with lime–sand mortar. Consequently, when the hut walls collapsed, one of the cauldron surfaces remained in contact with the ground whereas the other was buried by wall debris—which was rich in calcium carbonate and corroded the alloy to form malachite. The other side of the cauldron was in contact with chloride-rich earth, which caused the formation of atacamite instead.

Acknowledgements

The authors wish to acknowledge funding of this work by Spain's Ministry of Science and Education (Projects MAT 2013-44463-R and HAR 2013-43683-P), Junta de Andalucía and FEDER funds. The authors acknowledge the support of Rocío Otero from Nanochemistry and Fine Chemistry Research Institute (IUIQFN) for XRF spectroscopy experiments.

References

- [1] P. T. Craddock. The composition of the copper alloys used by the Greek, Etruscan and Roman civilizations 3. The origins and early use of brass. *J. Archaeol. Sci.* 5 (1978) 1-16.
- [2] K. Kareem, S. Sultan, L. He. Fabrication, microstructure and corrosive behavior of different metallographic tin-leaded bronze alloys part II: Chemical corrosive behavior and patina of tin-leaded bronze alloys. *Mat. Chem. Phys.* 169 (2016) 158-172.

- [3] O. Oudbashi, S. M. Emami, H. Ahmadi, P. Davami. Micro-stratigraphical investigation on corrosion layers in ancient Bronze artefacts by scanning electron microscopy energy dispersive spectrometry and optical microscopy. *Herit. Sci.* 1 (2013) 1-10.
- [4] O. Oudbashi. Multianalytical study of corrosion layers in some archaeological copper alloy artefacts. *Surf. Interf. Anal.* 47 (2015) 1133-1147.
- [5] A. Mezzi, E. Angelini, C. Riccucci, S. Grassini, T. De Caro, F. Faraldi, P. Bernardini. Micro-structural and micro-chemical composition of bronze artefacts from Tharros (Western Sardinia, Italy). *Surf. Interf. Anal.* 44 (2012) 958-962.
- [6] R. L. Frost. Raman spectroscopy of selected copper minerals of significance in corrosion. *Spectrochim. Acta A* 59 (2003) 1195-1204.
- [7] F. Di Turo, N. Montoya, J. Piquero-Cilla, C. De Vito, F. Coletti, G. Favero, A. Domenech-Carbó. Archaeometric analysis of Roman bronze coins from the Magna Mater temple using solid-state voltammetry and electrochemical impedance spectroscopy. *Anal. Chim. Acta* 955 (2017) 36-47.
- [8] J. Mathiyasara, N. Palaniswamy, V. S. Muralidharam. Corrosion resistance of cupronickels. An overview. *Corr. Rev.* 18 (2000) 65-103.
- [9] L. Birolo, A. Tomeo, M. Trifuoggi, F. Auriemma, L. Paduano, A. Amoresano, R. Vinciguerra, C. De Rosa, L. Ferrara, A. Giarra, A. Luchini, C. De Maio, G. Greco, A. Vergara. A hypothesis on different technological solutions for outdoor and indoor Roman wall paintings. *Archaeol. Anthropol. Sci.* 9 (2017) 591–602.
- [10] M. Iriarte, A. Hernanz, J. M. Gavira-Vallejo, J. Alcolea-González, R. de Balbín-Behrmann. μ -Raman spectroscopy of prehistoric paintings from the El Reno cave (Valdesotos, Guadalajara, Spain). *J. Archaeol. Sci: Reports* 14 (2017) 454-460.
- [11] R. Linn. Layered pigments and painting technology of the Roman wall paintings of Caesarea Maritima. *J. Archaeol. Sci: Reports* 11 (2017) 774-781.
- [12] D. Miriello, R. De Luca, A. Bloise, L. Dattola, G. Mantella, F. Gazineo, A. De Natale, M. T. Iannelli, F. A. Cuteri, G. M. Crisci. Compositional study of mortars and pigments from the “Mosaico della Sala dei Draghi e dei Delfini” in the archaeological site of

- Kaulonía (Southern Calabria, Magna Graecia, Italy). *Archaeol. Anthropol. Sci.* 9 (2017) 317–336.
- [13] A. C. Municchia, F. Bellatreccia, G. D'Ercoli, S. Lo Mastro, I. Reho, M. A. Ricci, A. Sodo. Characterization of artificial patinas on bronze sculptures of the Carlo Bilotti Mussem (Rome). *Appl. Physics A* 122 (2016) 1-8.
- [14] M. Quaranta, E. Catelli, S. Prati, G. Sciutto, R. Mazzeo. Chinese archaeological artefacts: Microstructure and corrosion behavior of high-leaded bronzes. *J. Cult. Her.* 15 (2014) 283-291.
- [15] C. Soffritti, E. Fabbri, M. Merlini, G. L. Garagnani, C. Monticelli. On the degradation factors of an archaeological bronze bowl belonging to a private collection. *Appl. Surf. Sci.* 313 (2014) 762-770.
- [16] P. Ropret, T. Kosec. Raman investigation of artificial patinas on recent bronze. Part I: climatic chamber exposure. *J. Raman Spectrosc.* 43 (2012) 1578-1586.
- [17] I. Constantinides, A. Adriaens, F. Adams. Surface characterization of artificial corrosion layers on copper alloy reference materials. *Appl. Surf. Sci.* 189 (2002) 90-101.
- [18] L. D. Mateos, D. Cosano, M. Mora, I. Muñiz, R. Carmona, C. Jiménez-Sanchidrián, J. R. Ruiz. Raman microspectroscopic analysis of decorative pigments from the Roman villa of El Ruedo (Almedinilla, Spain). *Spectrochim. Acta A* 151 (2015) 16-21
- [19] D. Cosano, L. D. Mateos, C. Jiménez-Sanchidrián, J. R. Ruiz. Identification by Raman microspectroscopy of pigments in seated statues found in the Torreparedones Roman archaeological site (Baena, Spain). *Microchem. J.* 130 (2017) 191–197.
- [20] D. Vaquerizo, F. Quesada, J. Murillo. *Protohistoria y romanización en la Subbética cordobesa*. Sevilla, Junta de Andalucía. 2001.
- [21] F. Quesada, I. Muñiz, I. López. La guerre et ses traces: destruction et massacre dans le village ibérique du Cerro de la Cruz (Córdoba) et leur contexte historique au II^e s. av. J.-C. In F. Cadiou; M. Navarro (eds.), *La Guerre et ses traces. Conflits et sociétés en Hispanie à l'époque de la conquête romaine (III^e e-I^{er} s. a.C.)*. Bordeaux, Ausonius, *Mémoires* 37 (2014) 231-271.

- [22] C. Carsana. *Commento storico al libro II delle Guerre Civili di Appiano (parte I)*. Pisa: Edizioni ETS, 2007.
- [23] F. Quesada, E. Kavanagh, M. Lanz. Los molinos del yacimiento del Cerro de la Cruz (Almedinilla, Córdoba): clasificación y análisis de los ejemplares de época ibérica y emiral. *Spal* 23 (2014) 83-118.
- [24] J. Moralejo, E. Kavanagh, F. Quesada. Improntas vegetales en arquitectura e improntas de cestería en el yacimiento ibérico del Cerro de la Cruz (Almedinilla, Córdoba). *Lucentum* XXXIV (2015) 119-144.
- [25] X. L. Armada, X.L. ¿Carne, drogas o alcohol? Calderos y banquetes en el Bronce Final de la Península Ibérica. *Cuadernos de Prehistoria de la Universidad de Granada* 18 (2008) 125-162.
- [26] L. Robbiola, J. M. Blengino, C. Fiaud. Morphology and mechanisms of formation of natural patinas on archaeological Cu-Sn alloys. *Corr. Sci.* 40 (1998) 2083-2111.
- [27] D. A. Scott. A review of copper chlorides and related salts in bronze corrosion and as painting pigments. *Stud. Conserv.* 45 (2000) 39-53.
- [28] B. W. Vink Stability relations of malachite and azurite. *Miner. Mag.* 50 (1986) 41-47.
- [29] M. C. Bernard, S. Joiret, S. Understanding corrosion of ancient metals for the conservation of cultural heritage. *Electrochim. Acta* 54 (2009) 5199-5205.
- [30] S. Hou, Y. Li, M. Xie, T. R. M. De Beer, W. R. G. Baeyens, S. Hu, J. Ouyang. Investigation of patinas formed on Chinese bronzes using modern multianalytical techniques. *Surf. Interf. Anal.* 39 (2007) 775-782.
- [31] M. L. Young, F. Casadio, J. Marvin, W. T. Chase, D. C. Dunand. An ancient Chinese bronze fragment re-examined after 50 years: contributions from modern and traditional techniques. *Archaeometry* 52 (2010) 1015-1043.
- [32] T. Pagnier, M. Boulova, A. Galerie, A. Gaskov, G. Lucazeau. Reactivity of SnO₂-CuO nanocrystalline materials with H₂S: a coupled electrical and Raman spectroscopic study. *Sensor Act. B* 71 (2000) 174-179.
- [33] T. Kosec, P. Ropret, A. Legat. Raman investigation of artificial patinas on recent bronze. Part I: urban rain exposure. *J. Raman Spectrosc.* 43 (2012) 1587-1595.

- [34] M. Serghini-Idrissi, M. C. Bernard, F. Z. Harrif, S. Joiret, K. Rahmouni, A. Srhiri, H. Takenouti, V. Vivier, M. Ziani. Electrochemical and spectroscopic characterizations of patinas formed on an archaeological bronze coin. *Electrochim. Acta* 50 (2005) 4699–4709.
- [35] B. S. Yu, J. N. Fang, E. P. Huang. Characteristics of the Raman spectra of archaeological malachites. *J. Raman Spectrosc.* 44 (2013) 630-636.
- [36] J. Sun, Z. Wu, H. Cheng, Z. Zhang, R. L. Frost. A Raman spectroscopic comparison of calcite and dolomite. *Spectrochim. Acta A* 177 (2014) 158-162.
- [37] Y. Wang, D. C. Alsmeyer, L. McCreery. Raman spectroscopy of carbon materials: Structural basis and observed spectra, *Chem. Mater.* 2 (1990) 557-563.
- [38] L. Robbiola, J.-M. Blengino, C. Fiaud. Morphology and mechanisms of formation of natural patinas on archaeological Cu-Sn alloys. *Corr. Sci.* 40 (1998) 2083-2111.

Table 1. SEM–EDS results for each of the corrosion layers in Fig 4.

Layer	Element (atomic %)								
	Cu	Sn	Fe	Ca	Si	O	C	Cl	S
A	28	-	1	13	14	26	15	-	-
B	45	-	2	5	10	21	8	-	-
C	60	4	-	1	5	20	-	3	2
D	53	6	1	2	6	16	-	8	-

Table 2. Chemical composition of the cauldron measured by XRF (%).

Component	Mass (%)
MgO	1,39
Al ₂ O ₃	2,68
SiO ₂	17,10
S	0,26
Cl	3,81
CaO	7,96
Fe ₂ O ₃	1,26
Cu	53,62
Sn	8,63
Sb	1,45
Others (P, K, Pb, Hf, Ag, Sr, As)	1,84

Fig 1. Reconstructed profile and volume for the bronze cauldron.

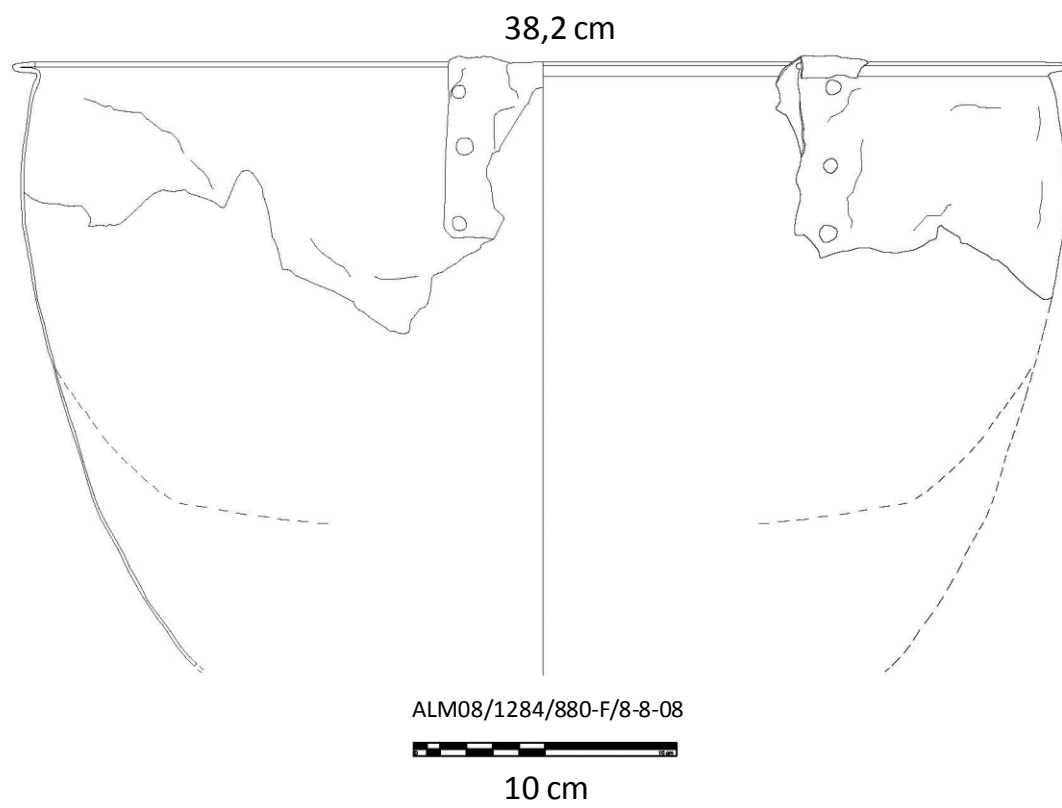


Fig 2. Cauldron elements (a), adhered debris (b) and repairs (c).

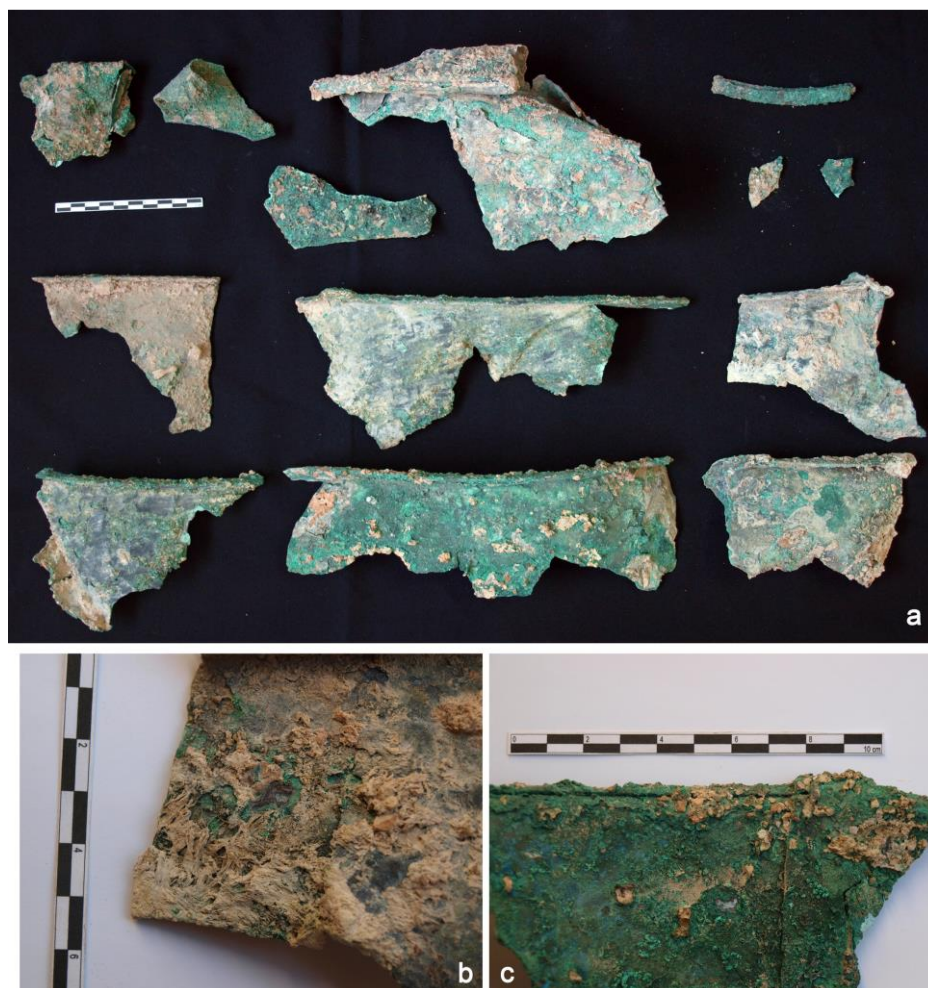


Fig 3. Cross-sectional micrograph of one of the fragments found at the Iberian site of Cerro de la Cruz (Almedinilla, southern Spain).

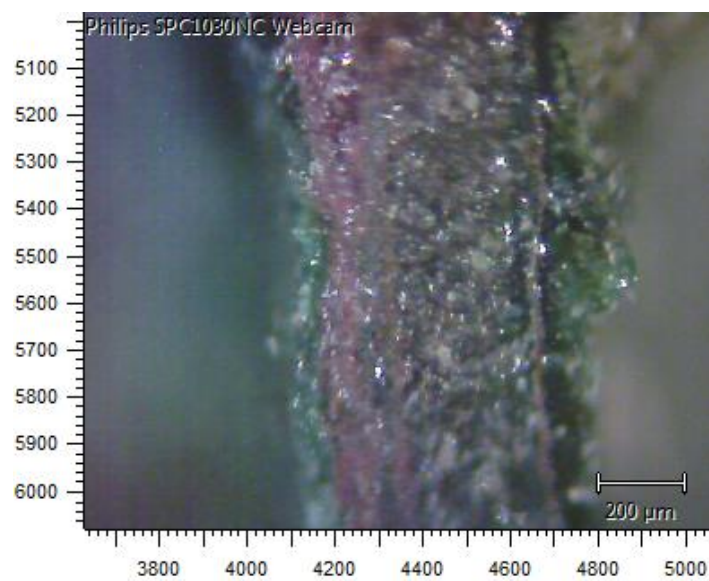


Fig 4. Image of a fragment as obtained under scanning electron microscope.

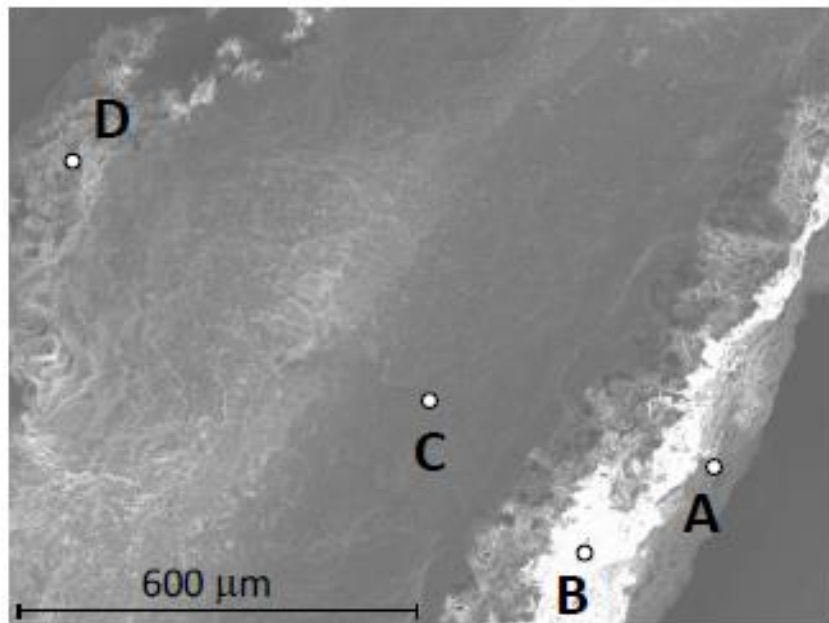


Fig 5. XRF of tin distribution along a line: (a) Outer layer containing less adhered debris; (b) reddish inner layer; and (c) green-greyish outer layer with abundant adhered debris.

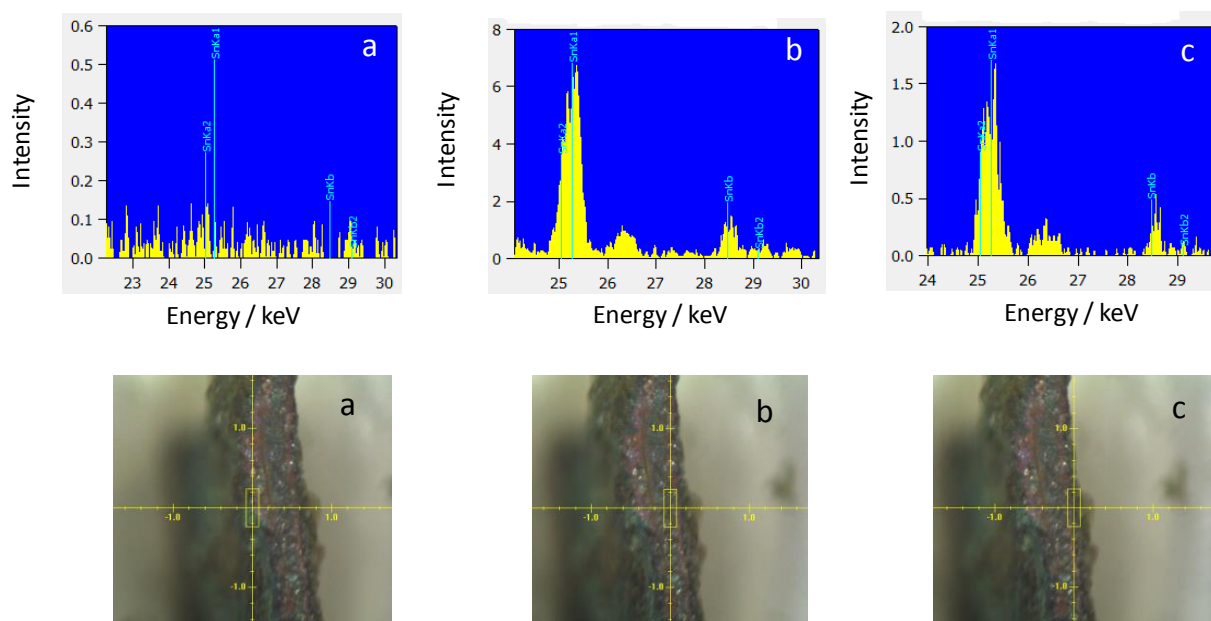


Fig 6. XRD patterns for powdered samples from a cauldron fragment.

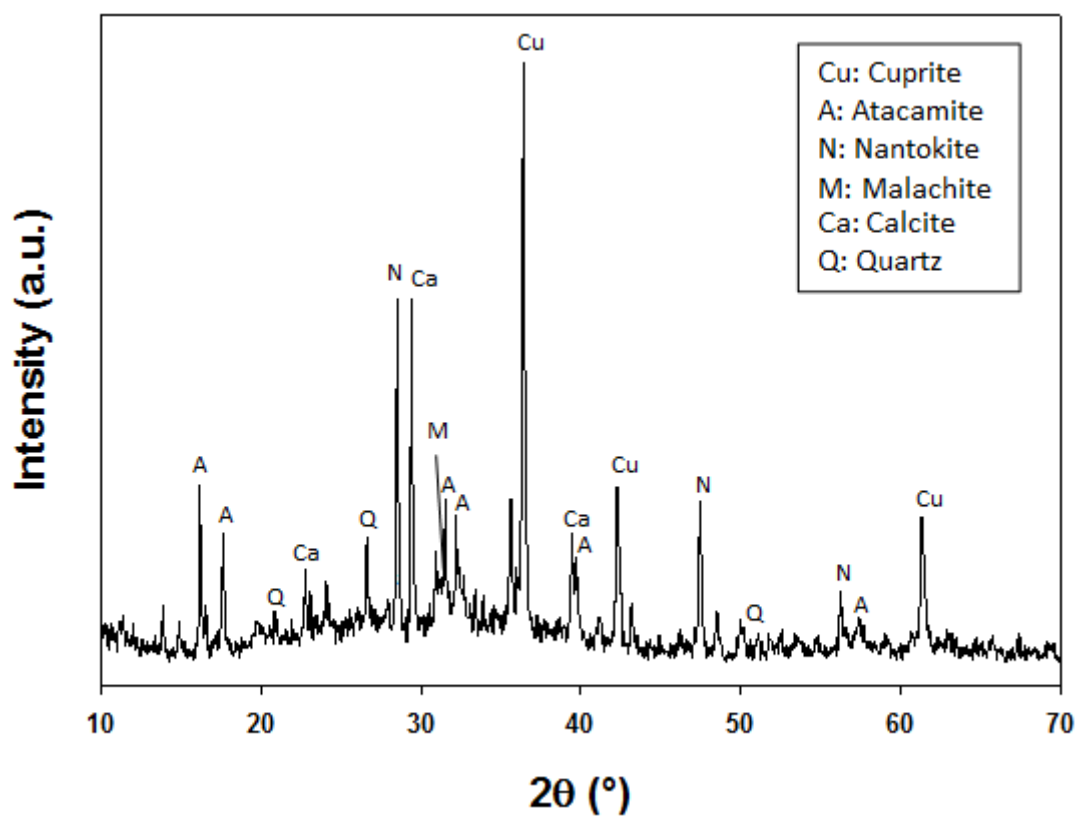


Fig 7. XRD patterns for the sides containing little (a) and abundant adhered debris (b) in one of the fragments.

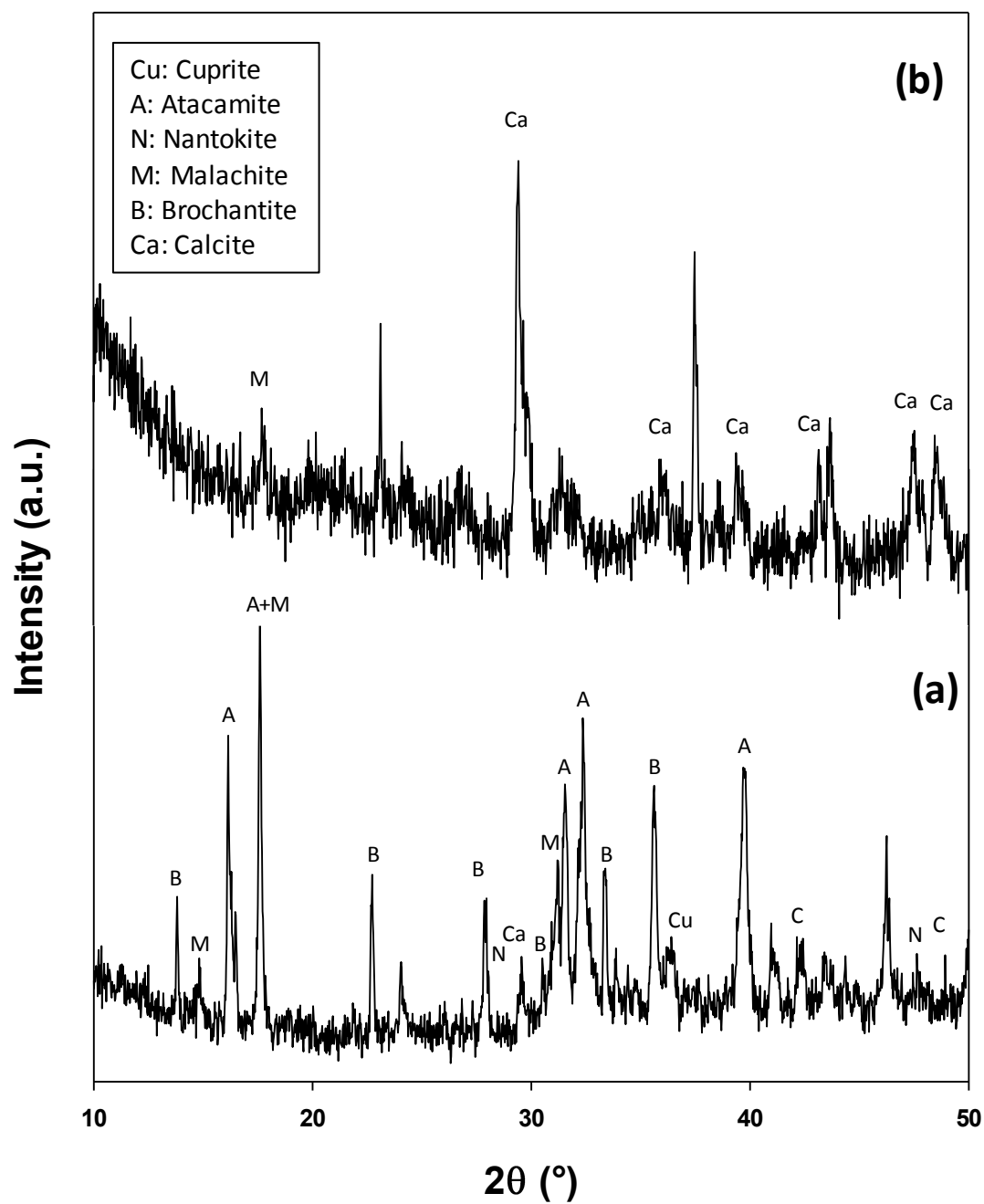


Fig 8. Raman spectrum for the red cross-sectional stratum in one of the fragments.

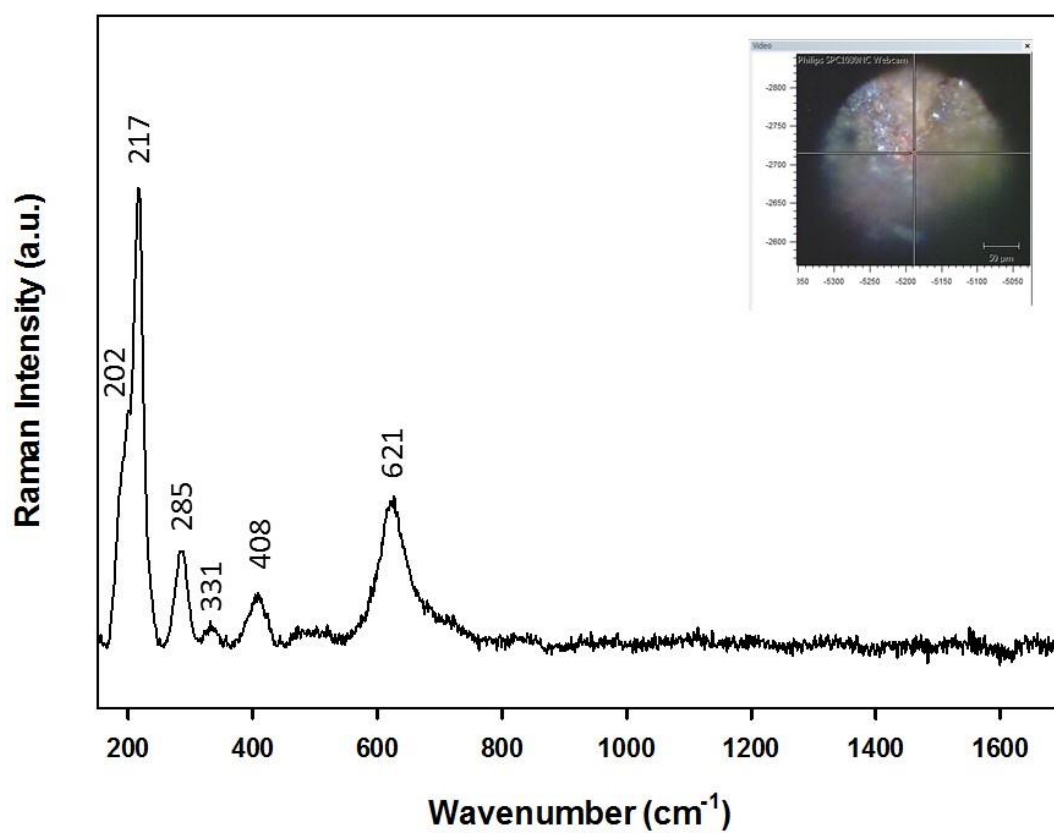


Fig 9. Raman spectrum for the green cross-sectional stratum in a fragment containing no debris.

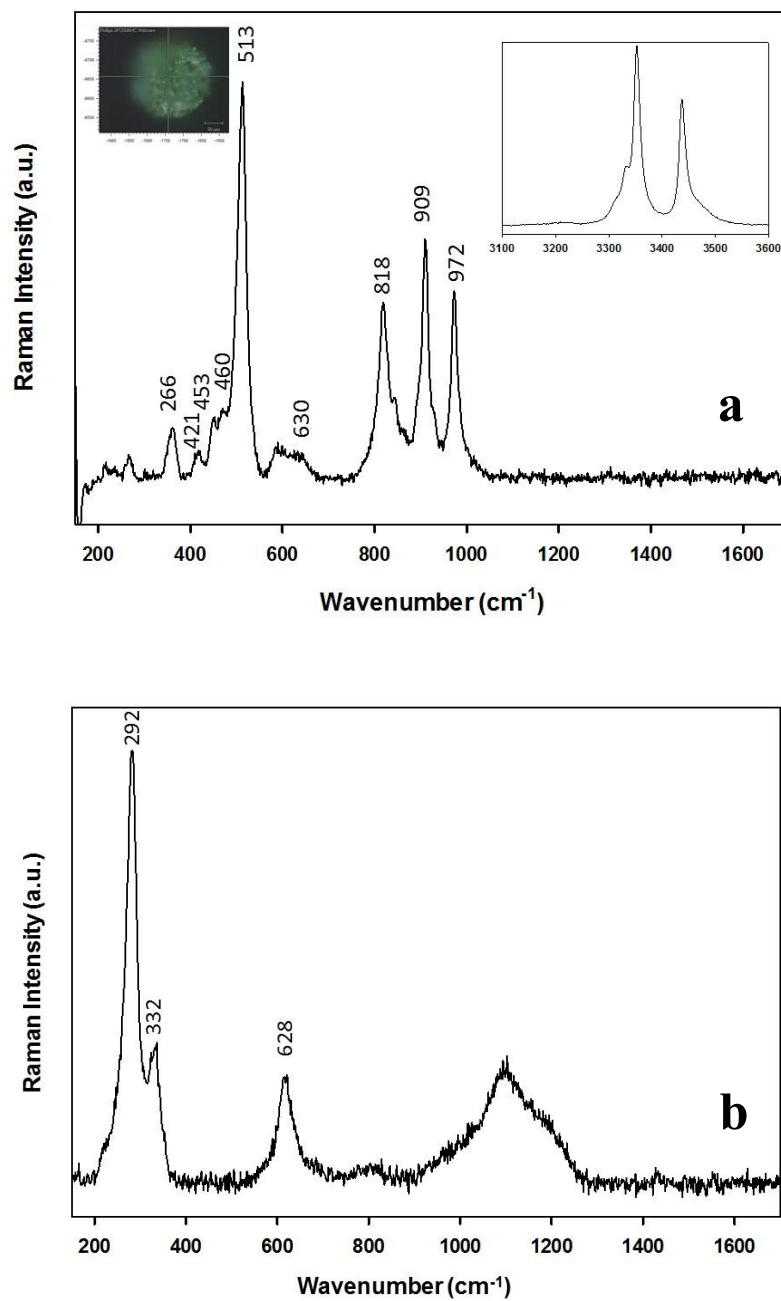


Fig 10. Raman spectrum for the side containing a large amount of adhered debris.

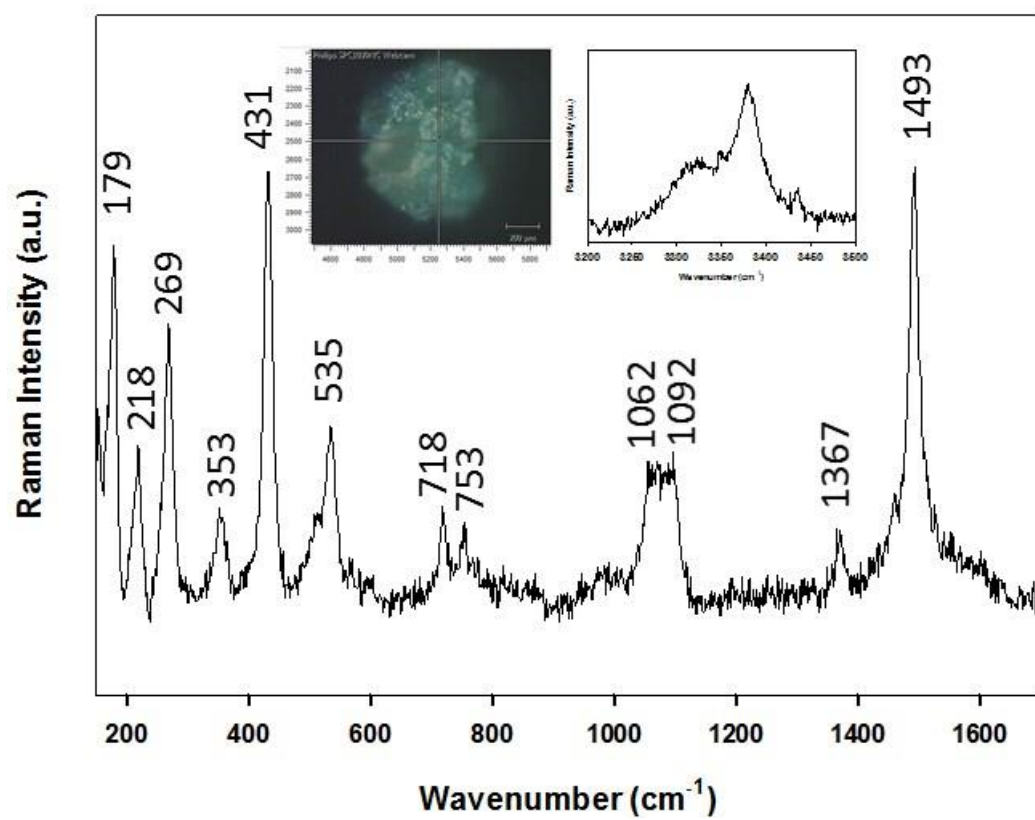


Fig 11. Raman spectra for the white (a) and black zones (b) of the fragment side containing a large amount of debris.

